Vacuum 214 (2023) 112146

Contents lists available at ScienceDirect

Vacuum

journal homepage: www.elsevier.com/locate/vacuum

Development of a lanthanum hexaboride hollow cathode for a magnetic octupole thruster

Jordan H. Hsieh [a], Mitchell M. Shen [b], Yueh-Heng Li [a,c,*], Ping-Han Huang [a]

[a] Department of Aeronautics and Astronautics, National Cheng Kung University, Tainan, 70101, Taiwan
[b] Department of Astrophysical Sciences, Princeton University, Princeton, NJ, 08544, USA
[c] International Doctoral Degree Program on Energy Engineering, National Cheng Kung University, Tainan, 70101, Taiwan

ARTICLE INFO

Handling Editor: Prof. L.G. Hultman

Keywords:
Electric propulsion
Lanthanum hexaboride
Hollow cathode
Magnetic octupole plasma thruster
Octupole magnetic field

ABSTRACT

Electric propulsion has undergone significant advancements, leading to increased usage in satellite constellation management and orbital transfer vehicles. This study describes the design and development of a lanthanum hexaboride (LaB6) hollow cathode for the Magnetic Octupole Plasma Thruster (MOPT), a novel electric propulsion concept for future space missions. Its operational characteristics are also provided. To gain insights into the coupling behavior between the cathode plume and the octupole magnetic field, the hollow cathode was operated with and without an octupole magnet over a range of discharge currents and flow rates. The results indicate that the discharge voltage was anti-correlated with the discharge current and flow rate. Notably, the octupole magnetic field observed reduced discharge voltage oscillations in both high- and low-discharge-current regimes. Nonetheless, the existence of the magnetic field was associated with the amplification of ionization-like instabilities in the high-flow-rate regime. Finally, the paper also delves into the plasma behavior under the influence of the octupole magnetic field, signifying an advancement in developing LaB6 hollow cathodes for their potential use in space-based MOPT applications.

1. Introduction

The decline in space launch costs and the ability to miniaturize satellites have increased the number of low Earth orbit constellations and prompted the development of electric propulsion (EP) systems with high performance and long-life capabilities [1–9]. Low-thrust and low-power EP systems, such as field emission electric propulsions, pulsed plasma thrusters [4,7,10–12], and vacuum arc thrusters [9,13], are commonly used for orbital control in nanosatellites and for attitude determination and control system desaturation in geostationary equatorial orbit satellites [10,14,15]. By contrast, high-thrust and high-power EP systems, such as Hall thrusters [2], ion thrusters [16,17], and magneto-plasmadynamic thrusters, are commonly used for orbit transfer, inclination correction, station keeping, deorbiting, and collision avoidance in small to large satellites.

Most EP systems require cathodes to emit electrons to neutralize the ion beam ejecting from the thruster, thereby maintaining the satellite's neutrality. Hall thrusters and direct-current (DC) discharge ion thrusters require hollow cathodes (HC) to ionize the propellant gas and generate plasma for thruster operation. Lanthanum hexaboride (LaB6) HCs have been used in numerous research and space missions due to their extreme robustness and resistance to propellant impurities [18–30]. Because the evaporation rate of LaB6 is lower than that of refractory metals and impregnated dispensers at thermionic emission temperatures, LaB6 HCs have a longer operating lifetime than other cathodes [31,32].

In the context of HC operation, there exist two modes of discharge: spot mode and plume mode. The spot mode is a stable and relatively quiescent mode of discharge that forms a plasma ball or spot downstream of the cathode exit. On the other hand, the plume mode is a precarious mode characterized by a widely diverging plasma cone that extends from the cathode and fills the vacuum chamber with diffuse plasma. The transition from the spot mode to the plume mode is an area of great interest in the study of cathode physics as it is associated with an ionization-like instability that can generate energetic ions and enhance cathode erosion [33]. However, it has been observed that the amplitude of the ionization instability decreases with higher field strengths in the presence of an applied magnetic field, which simulates the Hall thruster environment [34]. This reduction in instability suggests the potential for other instabilities to arise in the plasma under these conditions. For instance, drift instability has been reported to propagate azimuthally

* Corresponding author. Department of Aeronautics and Astronautics, National Cheng Kung University, Tainan, 70101, Taiwan.
E-mail addresses: yueheng@mail.ncku.edu.tw, yuehheng.li@gmail.com (Y.-H. Li).

https://doi.org/10.1016/j.vacuum.2023.112146
Received 15 March 2023; Received in revised form 30 April 2023; Accepted 1 May 2023
Available online 10 May 2023

across the magnetic field lines [34–36], namely rotating oscillations, and kink instability can occur at high discharge currents [37].

The Magnetic Octupole Plasma Thruster (MOPT) operates similarly to a Hall thruster with a centrally mounted HC but employs a line-cusp magnetic field configuration. Considering the HC will be mounted along the center axis of the MOPT, the discharge characteristics and performance of HCs influenced by an octupole magnetic field should be investigated in advance. This study aims to fill the gap in the literature concerning the discharge profile of HCs in the presence of an octupole magnetic field, focusing on characterizing the steady-state discharge voltage and current, plume mode oscillation, and current-driven instabilities. Despite the importance of these phenomena in understanding the performance of HCs, they have not been extensively researched in the literature. Additionally, this study describes the design and development of the LaB6 HC, which follows the classical cylindrical HC design proposed in Ref. [38], which utilizes a graphite keeper and cathode tube with a thermionic emitter located along the center axis. According to the estimation, the MOPT is projected to operate within a discharge voltage range of 150–350 V and a discharge current of 5–9 A; this indicates that the HC design must supply sufficient electrons up to 9 A to achieve stable MOPT operation and be self-sustaining, i.e., operate in the self-heating mode, at its nominal flow rate within this discharge current range.

This paper is organized as follows. Section 2 describes the concept of a MOPT. Section 3 illustrates the cathode design and the experimental setup and procedure. Section 4 presents the experiment results and details the plasma behavior within the cathode and plume regions. Finally, section 5 concludes the study.

2. Magnetic Octupole Plasma Thruster

The MOPT design is inspired by the operating principle of Hall thrusters [39–45], and the magnetic field topology of synchrotron storage rings [46], which aims to simplify the design and reduce the volume of Hall thrusters. The MOPT operates on the principle of replacing the conventional magnetic circuit of the Hall thruster with an octupole magnetic field formed by eight permanent magnets and a magnet yoke, thus forming a closed-loop magnetic circuit. Similar to Hall thrusters, the MOPT requires an external electron source to ionize the propellant in the discharge channel. Fig. 1 depicts the configuration of the MOPT with a HC mounted internally, where $\vec{B}$ denotes the magnetic field and $\vec{E}$ denotes the electric field.

After heating the LaB6 emitter to its thermionic temperature, sufficient for ignition, neutral gas is injected into both the cathode and the thruster. The keeper and anode are positively biased compared to the emitter to initiate cathode ignition. After the cathode discharges, the plasma potential extracts electrons directly from the insert region to the anode, which ionizes the neutral gas propellant within the discharge chamber. Applying an octupole magnetic field increases the electron drift resistance, which, in turn, can increase the ionization rate of the neutral propellant. The accelerated ions create thrust by passing through the strong electric field in the discharge chamber, formulated by the anode and trapped electrons. A portion of the electrons provided by the cathode neutralizes the leaving ion beam, thereby maintaining the thruster's neutrality. The MOPT's magnetic field interacts with the plasma throughout the cathode's insert, orifice, and plume regions, playing a crucial role in determining the cathode plume and plasma formation process. The following sections will discuss the interaction of cathode plasma with the octupole magnetic field.

3. Experimental design

3.1. Cathode design

A cylindrical Lab6 insert made of pressed and sintered LaB6 powder was inserted into the HC to enable thermionic emission J, which is well described by the Richardson–Dushman equation as follows [18]:

$$J = AT^2 e^{\frac{-e\varnothing_{wf}}{kT}}, \tag{1}$$

where A is a theoretical coefficient in the Richardson–Dushman equation, T is the temperature in K, e is the elementary charge, $\varnothing_{wf}$ is the work function in the unit of eV, and k represents Boltzmann constant. Fig. 2 displays a schematic of the HC of the MOPT. The heater surrounding the graphite cathode tube comprised 20 alumina tubes and 2

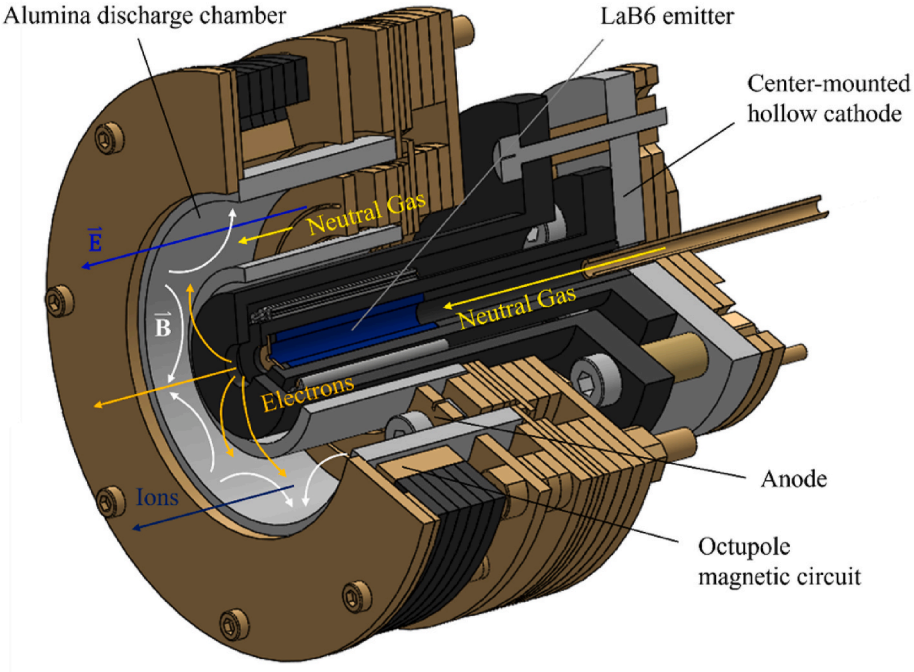

Fig. 1. Configuration of the MOPT with a center-mounted HC.

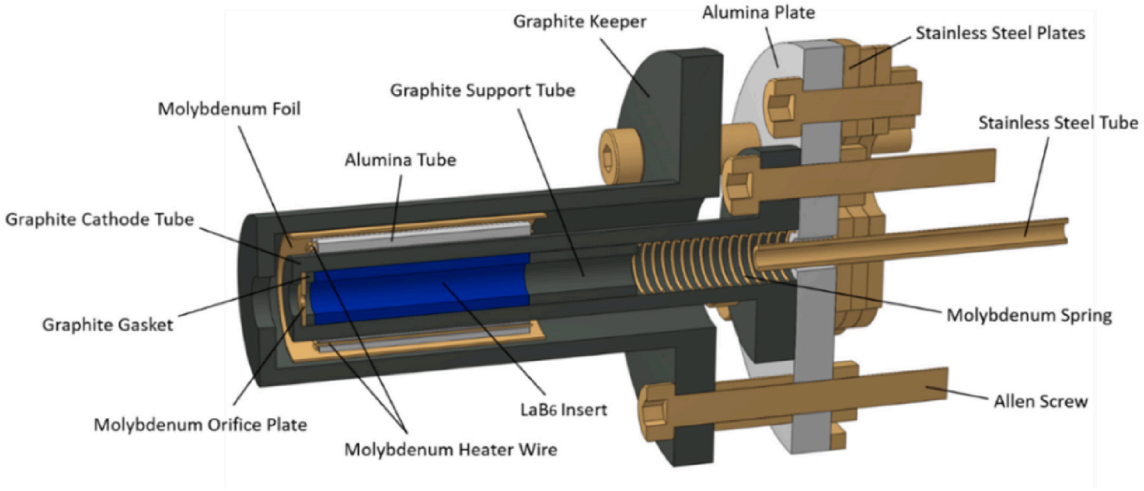

Fig. 2. Cross section of the hollow cathode.

parallel molybdenum heater wires, and an alumina plate was used for electrically isolating the keeper and cathode tube.

Because boron tends to diffuse from LaB6 to most refractory metals at high temperatures, thereby weakening the supporting material that can be used at the operating temperature of LaB6, graphite was used to construct the cathode tube to inhibit boron diffusion [47]. In addition, mechanical stress and thermal shock might cause LaB6 to fracture; thus, graphite is a suitable candidate for constructing the cathode tube because its coefficient of thermal expansion is similar to that of LaB6. Photographs of the cathode with and without a keeper are displayed in Fig. 3.

The orifice plate utilized in this study is composed of molybdenum, with a thickness of 0.5 mm and a diameter of 1 mm. The keeper is designed with an open aperture size of 6 mm and an orifice length of 2 mm. The keeper has an outer diameter of 20 mm and an inner diameter of 16 mm. The inner diameter of the cathode tube is 6.35 mm, which matches the outer diameter of the emitter. The emitter has an inner diameter of 3.8 mm and a length of 25 mm. The standoff distance between the orifice plate and the keeper is 3 mm. Five turns of molybdenum foil are wrapped around the heater to reduce heat loss through radiation. The inner diameter of the keeper restricted the number of turns of the molybdenum radiation shield. In addition, the molybdenum spring pushing against the alumina base plate reduced the contact area between the cathode and the alumina base plate, thereby considerably decreasing heat loss through conduction.

3.2. Experimental setup

Fig. 4 illustrates the experimental setup used in this study. The cathode was mounted on a supporting frame made of extruded aluminum (C) and tested in an EP operation chamber (A) with a human-machine interface controller (N) at NCKU. A stainless-steel cylinder with a diameter of 0.64 m and a length of 0.76 m was used to create a vacuum environment within the chamber, which was then pumped by an Agilent dry pump (J) and a HIPace turbo-molecular pump (O).

A water-cooling system (K) maintained the turbo-molecular pump at room temperature. The base pressure of the chamber was maintained within 10^{-5} Torr and 10^{-4} Torr at a maximum argon flow of 7 standard cubic centimeters per minute (SCCM). The argon flow rate was controlled using a 10-SCCM mass flow controller (H, I), and the adopted propellant was 5N2-grade argon with 99.9992% purity (E).

Two temperature input devices (F) were used to transmit R-type thermocouple data to a laptop (G) to monitor temperature fluctuations. The BK MR50040 (M), BK DS6024 (B), and IDRC DSP-HD (L) DC power supplies were used for the anode, heater, and keeper, respectively. A Teledyne LeCroy HDO4000A oscilloscope (D) was used to draw the cathode discharge *I–V* curve. Fig. 5 depicts the HC assembly mounted in a vacuum chamber. Fig. 5(a) and (b) depict the cathode with and without an octupole magnet. The octupole magnet comprised eight SmCo magnets, which can generally withstand extreme temperatures. However, the magnets were wrapped with brass foil as a redundant radiation shield to ensure that the temperature did not exceed the permissible threshold because of the intense radiation emitted by the keeper. A cylindrical brass anode with an inner diameter of 38 mm, a thickness of 2 mm, and a length of 100 mm was then placed 10 mm in front of the keeper. Notably, the geometry of the anode and its location with the cathode altered the entire experimental discharge profile [48, 49].

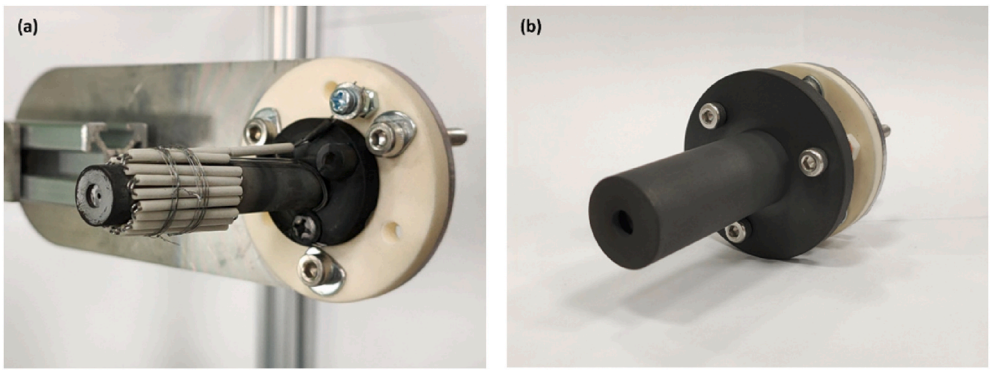

Fig. 3. Hollow cathode (a) without and (b) with a keeper.

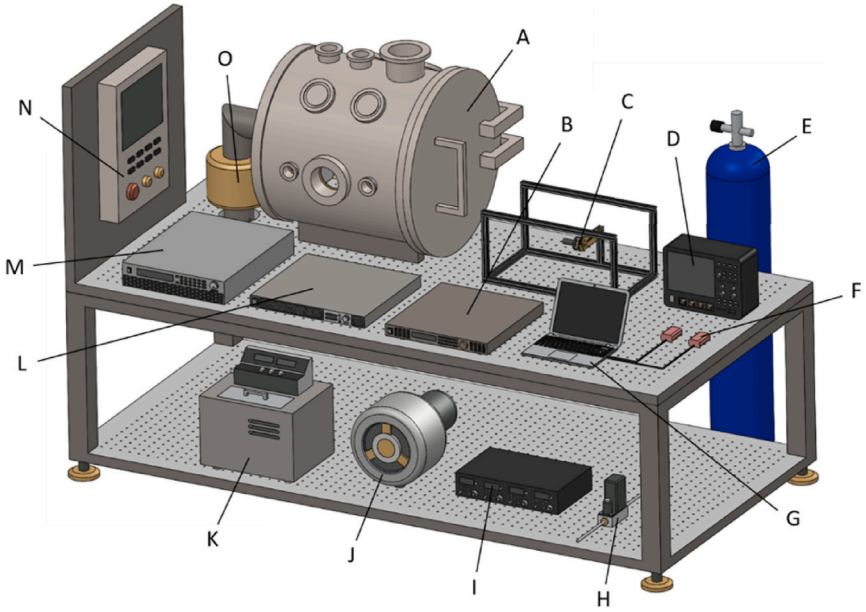

A	Electric Propulsion Operation Chamber	**H、I**	Mass flow controller
B	BK DS6024 power supply	**J**	Agilent dry pump
C	Aluminum extrusion-made supporting frame	**K**	Water cooling system
D	Teledyne Lecroy HDO4000A oscilloscope	**L**	IDRC DSP-HD power supply
E	Argon gas cylinder	**M**	BK MR50040 power supply
F	Temperature input devices	**N**	Human-machine interface controller
G	Laptop	**O**	HIPace turbo-molecular pump

Fig. 4. Experimental setup with the EP operation chamber.

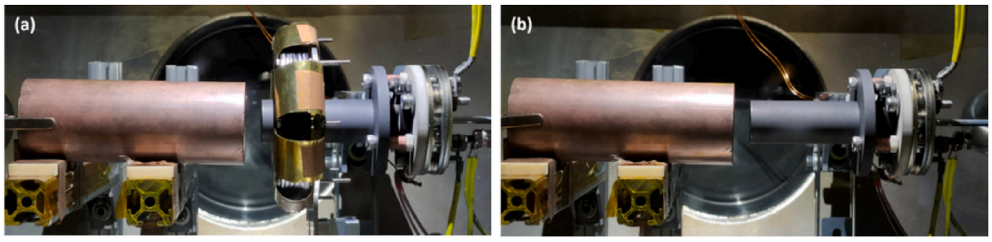

Fig. 5. Hollow cathode with the anode in a vacuum chamber (a) with and (b) without an octupole magnet.

3.3. Electrical circuit

Fig. 6 depicts the electrical connections used in the experiment. The cathode tube and each power supply were connected to the common ground of the test facility. The heater was powered by a programmable BK DS6024 DC power supply (0–60 V, 0–24 A). The discharge between the keeper and the LaB6 emitter was generated by a programmable IDRC DSP-HD DC power supply (0–600 V, 0–2.5 A). The discharge between the cylindrical anode and the emitter was maintained by a programmable BK MR50040 DC power supply (0–500 V, 0–10 A). All of the aforementioned electrical circuits were connected using Teflon shielded wire in the vacuum chamber to prevent outgassing from disrupting the experiment.

A Teledyne LeCroy HDO4000A oscilloscope (1 GHz) with four LeCroy PP020 voltage probes (500 MHz, 11 pF) was used to measure the cathode discharge *I–V* envelope. Voltage probes V_2 and V_4 were used to measure the keeper and anode potentials, respectively, which excluded the potential drop caused by the shunt resistor. Voltage probe V_1 was used to measure the shunt resistor and keeper–emitter potential, while voltage probe V_3 was used to measure the shunt resistor and anode–emitter potential. The anode and keeper currents were then calculated by subtracting the voltage probe readings. Considering that both the anode and keeper power supplies operated in control current mode, the current data were used only to verify the accuracy of the experimental results.

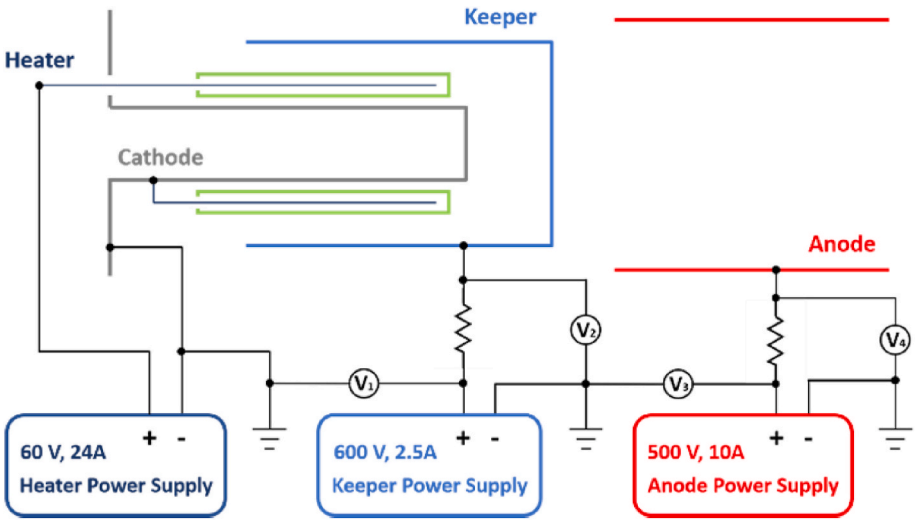

Fig. 6. Electrical circuit for cathode ignition and operation.

3.4. Experimental procedure

The standard procedure for igniting and operating the HC is described below. Different discharge currents and flow rates were selected to investigate the operational characteristics of the cathode. Before data collection, the cathode was warmed up for a few hours at a range of currents and flow rates before the discharge voltage became repeatable at a given operating point. The procedure for cathode ignition is as follows.

1. The argon flow rate is set to 7 SCCM for 10 min to purge the propellant supply lines.
2. The heater's power supply is activated with a maximum current of 7 A for 6 min. It is noted that the power supply constraint is to eschew the material cracking due to rapid thermal conductive expansion in the material.
3. After the temperature has reached a thermal equilibrium steady state (i.e., the temperature variation is within ± 1 °C), the heater current is increased by 0.1 A every 12 s for 1 min, followed by 7 min of dwelling to reach a steady state.
4. Repeat step 3 until the heater input power is approximately stabilized at 240 W (11 A, 21.8 V). At this instance, the molybdenum orifice plate should reach a temperature of approximately 1270 °C, monitored by the inserted four R-type thermocouples, as shown in Fig. 7.

Based on the test results, the heater's input power has been measured to reach 240 W upon reaching the working temperature of the HC. Furthermore, an external magnetic field has not been observed to affect the total heating power required for ignition. During the heating phase, four R-type thermocouples were used to characterize the thermal behavior of the cathode at four locations. Before the relevant experiment, each thermocouple was calibrated and coated with a thin layer of alumina to prevent chemical interactions and provide electrical isolation from the cathode surface. As shown in Fig. 7(a), considering the low thermal impedance between the orifice plate and the emitter, the TC-01 thermocouple was attached to the molybdenum orifice plate to provide a closer measurement of the emitter temperature.

Moreover, the TC-02 thermocouple was used to measure the temperature of the SPHC plate (i.e., magnetic yoke) to prevent the temperature from exceeding the maximum operating threshold of SmCo magnets. The TC-03 and TC-04 thermocouples were used on the keeper base frame and stainless-steel base plate, respectively. Fig. 7(b) depicts the thermal profile captured by each thermocouple. Notably, since no radiation loss compensation was performed, the measured temperature was marginally lower than the actual temperature. At the initial heating stage, the temperature of the molybdenum orifice plate (TC-01) and keeper base (TC-03) rapidly increased. However, at the post-heating stage, the rate of increase slowed down. This phenomenon was caused by the relatively low temperature, at which thermal conduction dominated heat loss. When the temperature reached 700 °C, the orifice plate

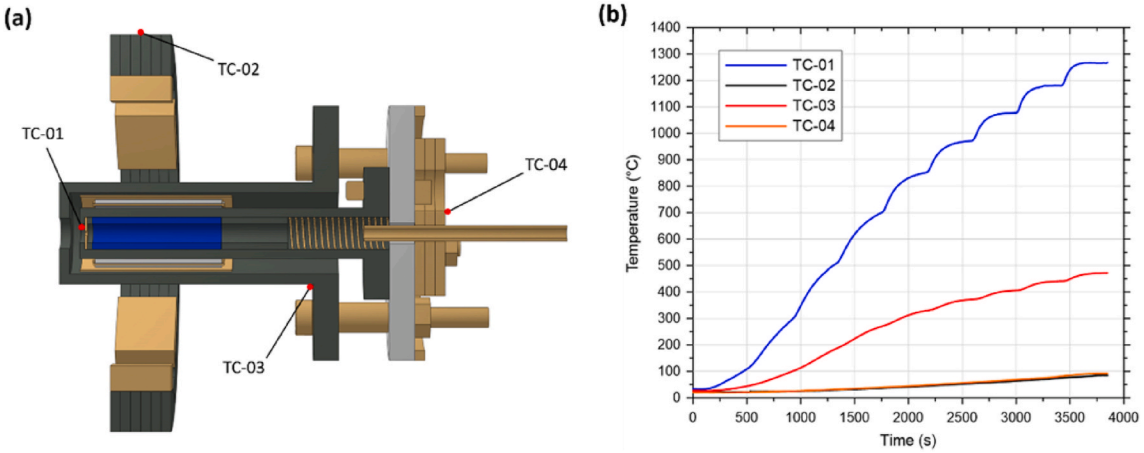

Fig. 7. (a) Measurement points for each thermocouple. (b) Temperature profile of each point.

(TC-01) and keeper base (TC-03) began to reach thermal equilibrium rapidly in each iteration because thermal radiation dominated the heat loss, which can be explained by the fact that the radiation emitted per unit time is directly proportional to the fourth power of temperature. Finally, at the cathode heating stage, the SPHC plates (TC-02) and stainless-steel base plates (TC-04) exhibited similar thermal behavior, which ensured that the temperature remained below 100 °C throughout the heating process.

After several experimental runs, the resistance of the molybdenum heater wire tended to increase naturally. This phenomenon can be ascribed to the formation of microcracks within the heater wire due to thermal fatigue, which decreases the cross-sectional area of the heater but increases its resistance. This fatigue might result in an excessively high-temperature hot spot of the heater wire, thereby degrading the lifetime of the HC.

After the emitter reaches its thermionic emission temperature, the experimental procedure is divided into two scenarios: (a) obtaining discharge voltage versus the discharge current and (b) characterizing the discharge voltage versus the propellant flow rate.

5. For (a) and (b), the anode and keeper voltages are set as 250 V, and the keeper current is set as 1 A. For (a), the initial anode current is set as 9 A, with the argon flow rate being 7 SCCM. For (b), the anode current is set as 8 A, with the argon flow rate being 6 SCCM. After the anode power supply is activated, the keeper power supply is activated.
6. After cathode ignition, the cathode plasma is directly coupled to the anode and keeper. Fig. 8 depicts the HC during discharge.
7. When the cathode breaks down, the keeper and heater power supplies are turned off. The cathode then operates in self-heating diode mode.
8. Capturing the discharge profile, which is stabilized after a few minutes of operation.
9. For (a), the anode current is reduced by 0.5 A but the argon flow rate is left unchanged. For (b), the argon flow rate is reduced by 1 SCCM but the same discharge current is left unchanged.
10. Steps 8 and 9 are repeated until the anode current reaches 6 A in (a) and the argon flow rate reaches the minimum value necessary to support cathode self-heating discharge in (b).

The same steps were followed for experiments with and without an octupole magnet to investigate the cathode performance when the cathode was coupled to an octupole magnetic field.

4. Results and discussion

4.1. Magnetic field simulation and measurement

An octupole magnet was placed 10 mm behind the keeper orifice to simulate the configuration of the MOPT with a center-mounted cathode. The octupole magnet comprises eight SmCo magnets and six stacked laser-cut hot-rolled sheet steel (SPHC) plates. These SmCo magnets are selected for magnetic field construction because of their high resistance to heat (300 °C) and high residual magnetism. Finite element method (FEM) analysis was then performed to simulate the magnetic flux density and topology.

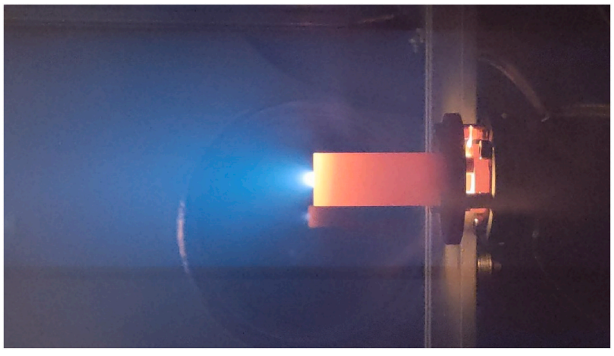

Fig. 8. Photograph of the hollow cathode operating at a discharge current of 9 A, with a flow rate of 7 SCCM.

In Fig. 9(a), the magnetic flux density and direction of the cross-sectional plane at the rotation angles of the octupole are presented. The magnetic field was examined at eight positions along the cathode axis, from the center of the insert to the plume region in front of the keeper, as displayed in Fig. 9(b) to 9(k). The magnetic field direction shown in Fig. 9(a) indicates a transverse magnetic field at the periphery of the keeper orifice, which will be used to explain the discharge characteristic in sections 4.3 and 4.4. It is worth noting that the maximum value of displaying the magnetic flux density was set to 50 Gauss for clarity, while the magnetic flux density may reach the order of 10^3 Gauss at the periphery of the octupole magnet. In Fig. 9(c) to 9(e), the simulation results indicate that the maximum magnetic flux density does not exceed 1.5 Gauss throughout the insert region, comparable to the geomagnetic field strength at the author's location. Therefore, it is conceivable that the octupole magnetic field's existence does not significantly impact the plasma properties in the insert region. Fig. 9(b) and (g) show the magnetic field direction and topology at the cross-sectional plane perpendicular to the cathode axis at the insert and plume regions, respectively.

After the simulation results of the cathode assembly provided information on the magnetic field, the magnetic profile was examined and verified using a Gauss meter with a transverse probe. Fig. 10(a) shows the measurement path for the transverse probe, which was 2 mm above one of the SmCo magnets. The transverse probe was positioned on a single-axis mobile platform with a resolution of 0.25 mm in each step. Fig. 10(b) presents the magnetic flux densities obtained through FEM analysis and measurements. The simulation results were validated to have a slight misalignment with the measurements, which might have been caused by several factors, such as measurement errors, machining tolerance deviations, and deviations of the magnetic profile provided by the supplier from the actual condition.

4.2. Cathode ignition

Upon reaching the emitter's thermionic temperature, the anode and keeper power supplies were activated, resulting in the discharge of the cathode. Fig. 11 displays the discharge and keeper voltages without the external magnetic field during the ignition process at 500 ms and 40 ms intervals. Based on the results obtained, no significant difference in the ignition profile was observed in the presence or absence of the external magnetic field. The anode and keeper voltages were set to 250 V to initiate ignition, while the anode current and keeper current were set to 9 A and 1 A, respectively. The flow rate of the gas was fixed at 7 SCCM. When the keeper voltage reached 28 V, voltage breakdown was observed, and the keeper voltage decreased to approximately 14 V for 23 ms. As shown in Fig. 11(b), after the voltage breakdown, the anode voltage decreased to approximately 45 V for 24 ms before stabilizing at 55 V in less than 30 ms. The keeper voltage eventually stabilized at 29 V. The keeper and heater power supplies were turned off 2 s after the cathode broke down, thus allowing the cathode to operate in a self-heating diode mode.

4.3. Plots of the discharge voltage versus the discharge current

Fig. 12 demonstrates the discharge voltage during steady operation versus the discharge current. The blue dots in this figure represent the discharge profile when the cathode operated without an octupole magnet, whereas the yellow dots represent the discharge profile when the cathode plasma was coupled to a magnetic field. At a gas flow rate of

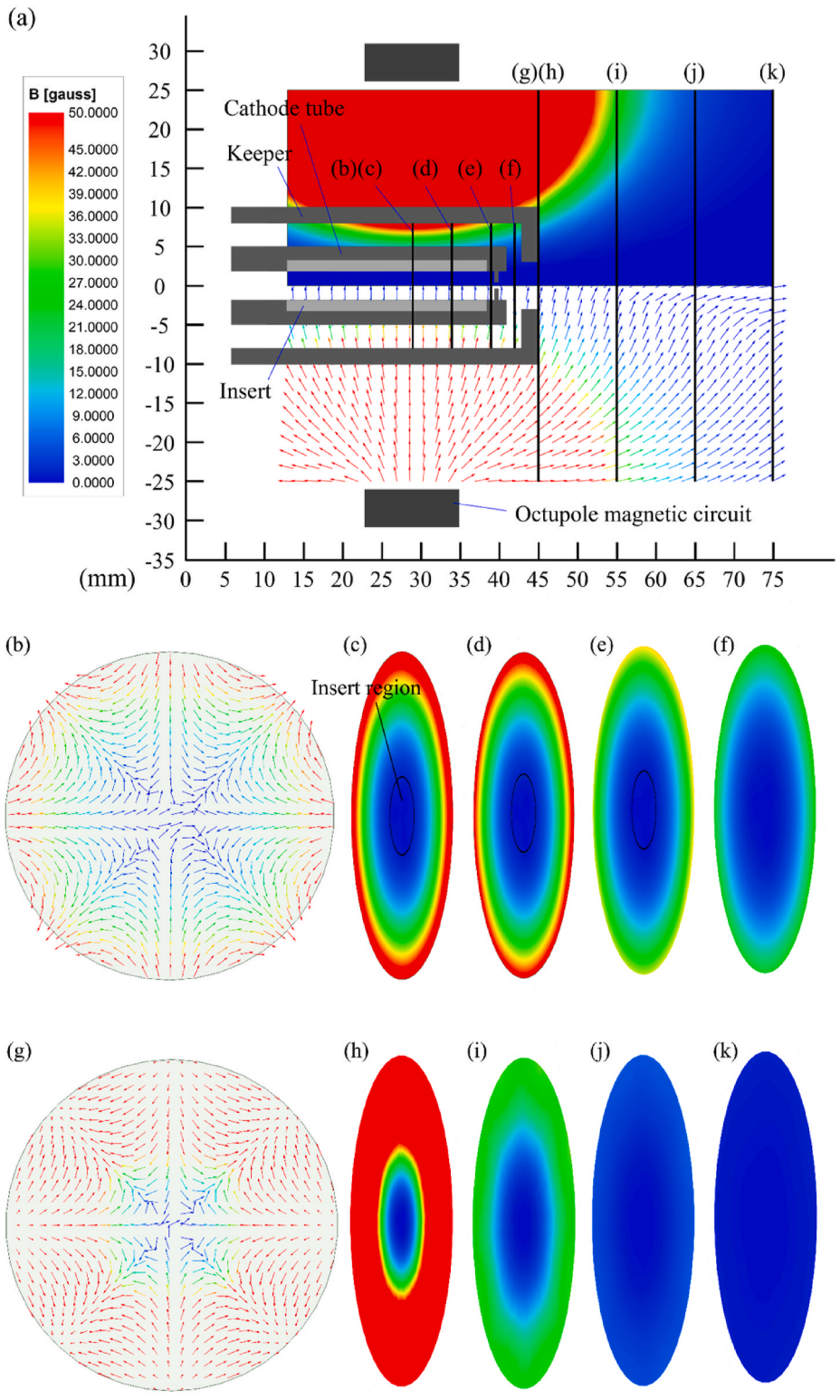

Fig. 9. FEM simulation results of an octupole magnet.

7 SCCM and without an external magnetic field, the discharge voltage of the HC was 50.7 V at a discharge current of 6 A. The discharge voltage decreased as the discharge current increased, reaching 26.2 V at a discharge current of 9 A. These results were consistent with previous studies [50,51] and can be explained by a reduction in the emitter sheath voltage [39,52]:

$$\varnothing_s = \frac{H(T)}{I_e} + \frac{5}{2}T_{eV} + \varnothing_{wf} - I_e R, \tag{2}$$

where $\varnothing_s$ is the cathode sheath voltage, $H(T)$ is the total heat loss of the insert because of radiation and conduction, I_e is the discharge current, T_{eV} is the electron temperature (in electron volts), $\varnothing_{wf}$ is the work function of the emitter, and R is the resistance. An increase in the

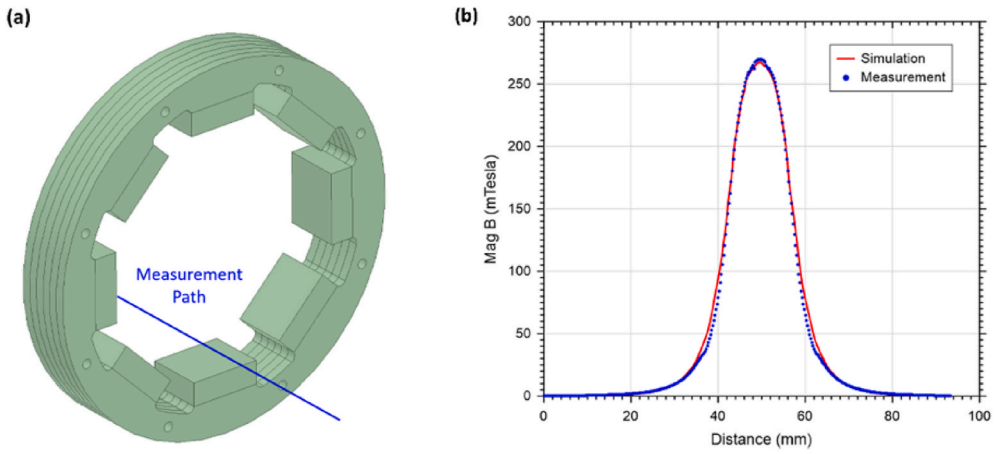

Fig. 10. (a) Measurement path for the transverse probe of the Gauss meter. (b) Magnetic flux densities obtained through FEM simulations and measurements.

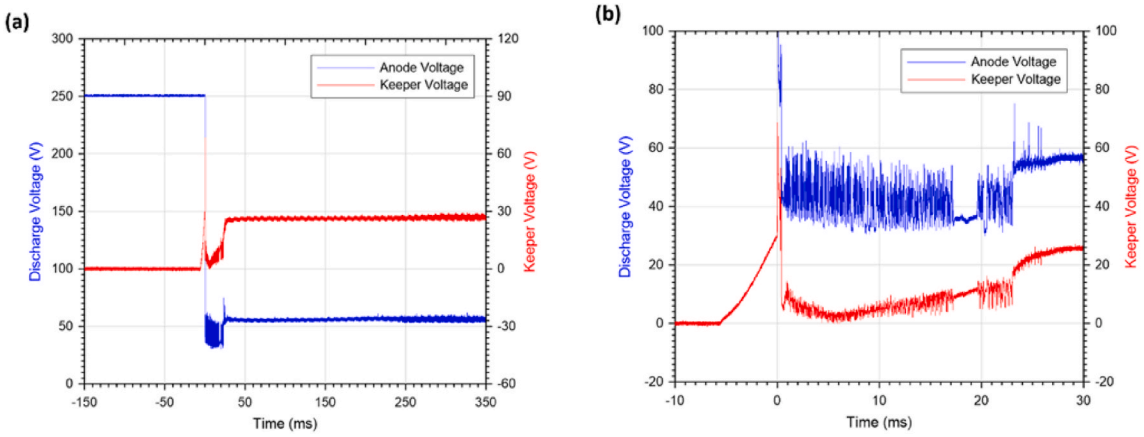

Fig. 11. Discharge and keeper voltages during ignition in (a) 500 ms and (b) zoom-in 40 ms traces.

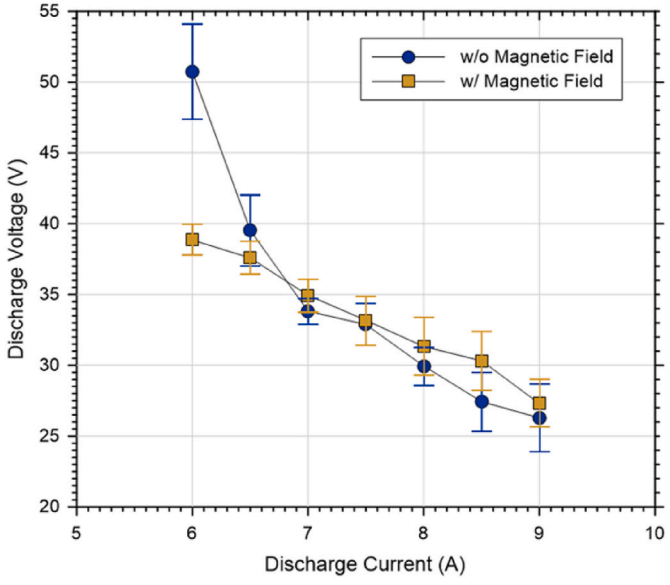

Fig. 12. Plot of the discharge voltage versus the discharge current at a nominal argon flow rate of 7 SCCM.

electron energy flux delivered to the emitter leads to an increase in the temperature of the emitter wall, thus increasing the density of the thermionic emission current required for an enhanced discharge current. A negative impedance trend can also be observed in the discharge profile of the HC when an octupole magnetic field is present. The discharge voltage of the cathode remains at 38.8 V for a discharge current of 6 A and subsequently decreases to 27.3 V when the discharge current increases to 9 A. Furthermore, the results presented in Fig. 12 indicate that the presence of an external magnetic field does not significantly affect the discharge voltage of the HC when the discharge current exceeds 7 A. However, the discharge voltage is noticeably different at lower discharge currents with and without the external magnetic field. The magnetic field simulation shows that the magnetic flux density in the insert region does not exceed 1.5 Gauss, comparable to the local geomagnetic field; this suggests that the magnetic field mainly affects the cathode plasma in the plume region rather than in the insert region. The difference in discharge voltage can be attributed to a small portion of low-energy electrons in the plume region trapped by the magnetic field. As a result, a slightly higher discharge voltage is required to sustain the main discharge. Fourier transform is employed to explain this disparity in the discharge voltage, as discussed later in this section.

In this study, discharge voltage fluctuations were characterized on the basis of the peak-to-peak voltage and discharge voltage oscillation amplitude. The discharge voltage oscillation amplitude Δ is defined as follows:

$$\Delta = \sqrt{\frac{\int_0^\tau (V_d - \overline{V}_d)^2 dt}{\tau}}, \tag{3}$$

where τ is the measurement time, V_d is the discharge voltage, and $\overline{V}_d$ is the average discharge current (i.e., $\overline{V}_d = \int_0^\tau V_d dt/\tau$). Here, amplitude was measured as the standard deviation of the discharge voltage, which is comparable to other studies of evaluating discharge current in Hall thrusters [2,53]. Fig. 13(a) depicts the peak-to-peak voltage with the discharge current. Similarly, Fig. 13(b) depicts the oscillation amplitude of the discharge voltage, exhibiting a similar trend to the peak-to-peak voltage.

In comparison to the peak-to-peak discharge voltage in the presence of an external magnetic field, the peak-to-peak discharge voltage without an octupole magnet increased by 9.9 V and 5.1 V at discharge currents of 6 A and 9 A, respectively. Furthermore, the amplitude of the discharge voltage oscillation was found to be 0.72 V higher at 9 A discharge current and 2.4 V higher at 6 A discharge current for the HC without an external magnetic field compared to the one with an external magnetic field. The time-varying waveforms and the discharge current power spectral density (PSD) at the discharge current of 6 A are shown in Fig. 14. Fig. 14(a) demonstrates that the absence of an external magnetic field results in low frequency and large amplitude oscillations in the discharge voltage, whereas the discharge voltage remains stable with the introduction of a magnetic field. Plasma oscillations in the cathode plume can be categorized into three primary groups based on frequency ranges [33,54]. The first group comprises power supply-induced oscillations, which occur at frequencies below 1 kHz. The second group comprises coherent, large-scale oscillations occurring in the near-field plume with frequencies below 150 kHz. Finally, the third group encompasses broadband, turbulent fluctuations with frequencies exceeding 200 kHz, often linked to the occurrence of ion-acoustic turbulence (IAT) [54]. The PSD analysis in Fig. 14(b) shows the presence of low-frequency but energetic discharge oscillations without a magnetic field in the range of 1–100 kHz, suggesting ionization-like instabilities in the cathode plume [49].

The significant peak-to-peak discharge voltage and amplitude of discharge voltage oscillation observed at low discharge currents without an octupole magnet can also be interpreted as an imbalance in the anode sheath current, as reported in previous studies [48,49,55,56]. The current flux of the cathode plasma was composed of thermionic electrons, thermal ions, and thermal electrons [57]. However, low plasma density cannot provide sufficient thermal electron current for the anode in the low-discharge-current regime. Therefore, the lack of steady-state thermal electrons could not sustain the discharge current required by the anode and form an electron-attracting sheath at the anode periphery to collect current. Consequently, an electron-attracting sheath was formed near the anode surface, accelerating electrons toward the anode. In Fig. 15, the high-energy electrons increased the secondary electron yield at the anode surface, causing more significant temporal fluctuations in the anode voltage, i.e., peak-to-peak discharge voltage and amplitude of discharge voltage oscillation. The decrease in voltage oscillation below 6.5 A discharge current in the HC with the presence of the magnetic field can be attributed to the transverse magnetic field in the plume region, as shown in Fig. 9. The electromagnetic field increases the path for electrons to reach the anode, which the electron drift velocity can be described as $\vec{v_d} = \vec{E} \times \vec{B}/B^2$, where E represents the electric field and B represents the magnetic field [58]. The increased path length leads to a higher ionization rate of neutral particles by collisions, which in turn provides more electrons to sustain the main discharge. Consequently, the discharge voltage does not increase significantly due to the sufficient electrons in the plume region.

Fig. 16 presents the time-varying waveform and PSD analysis at the discharge current of 9 A. A higher-density plasma and the formation of the IAT can explain the considerable anode potential fluctuation observed in the high-discharge-current regime in the absence of an octupole magnet [34,59–61]. The IAT is an electrostatic plasma instability that increases at the expense of the strong electron drift observed under a significant disparity between the ion and electron temperatures and a high electron drift velocity u_e. If the ion plasma frequency is considerably higher than the frequency of the waves in the IAT spectrum, the real and imaginary parts of the IAT dispersion relationship can be expressed as follows:

$$\omega_r = k(u_i + c_s) \equiv k v_g \tag{4}$$

$$\omega_i = k c_s \frac{u_e}{v_e} \equiv k c_s M_e, \tag{5}$$

where ω_r and ω_i are the real and imaginary parts of the wave frequency, respectively. k is the wave vector, u_i is the ion drift velocity, c_s is the ion-sound speed, v_g is the group velocity, v_e is the electron thermal velocity, and M_e is the electron Mach number. Equation (5) can be interpreted as the IAT being enhanced by the momentum contributed by fast electrons, a phenomenon which is referred to as inverse Landau damping.

According to Fig. 16(b), the PSD of the discharge voltage without the external magnetic field is higher than the one coupled with the magnet. The decrease in intensity of the broadband, turbulent fluctuations, i.e., the IAT, with frequencies exceeding 200 kHz in the high discharge

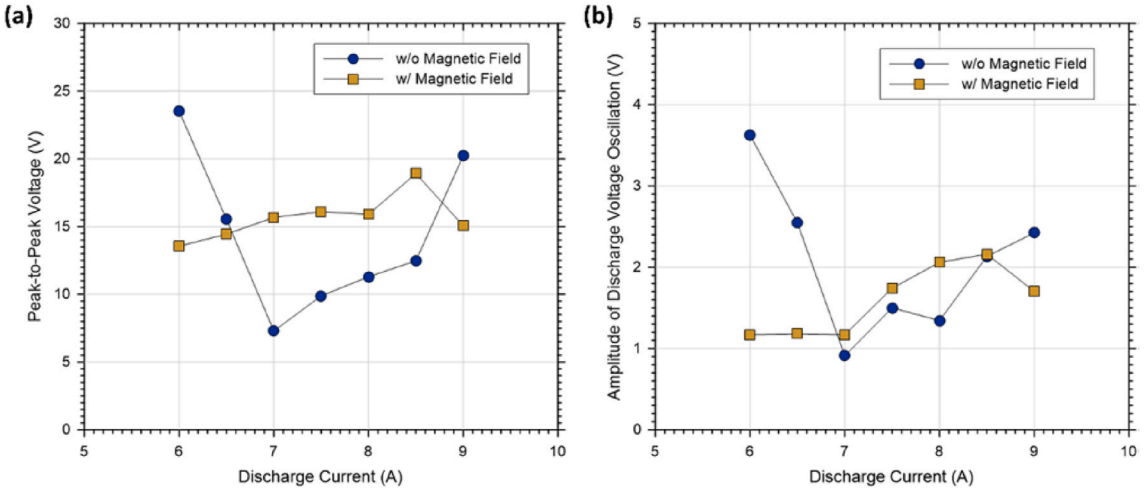

Fig. 13. Plots of the (a) peak-to-peak voltage and (b) amplitude of the discharge voltage oscillation versus the discharge current at a nominal argon flow rate of 7 SCCM.

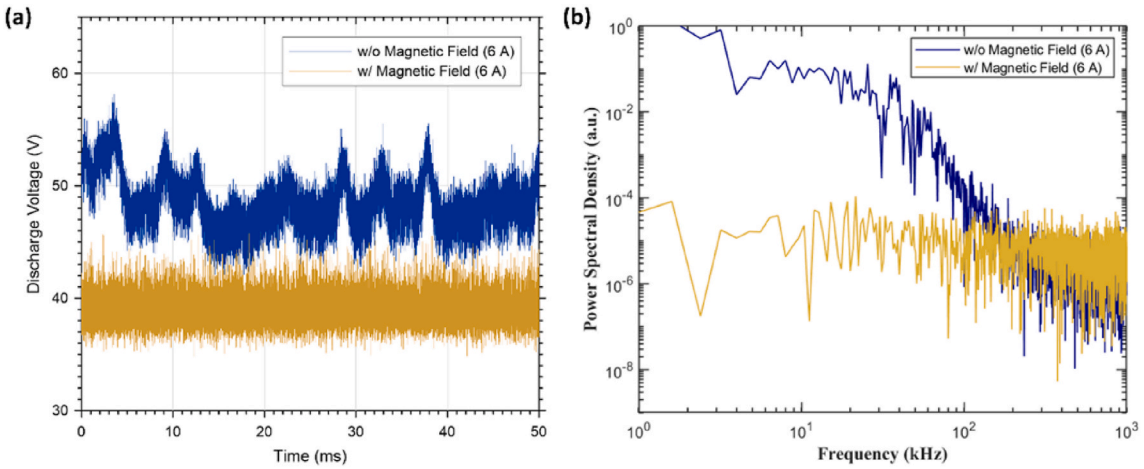

Fig. 14. Plots of (a) time-varying waveforms and (b) power spectral density at the discharge current of 6 A with the gas flow rate of 7 SCCM.

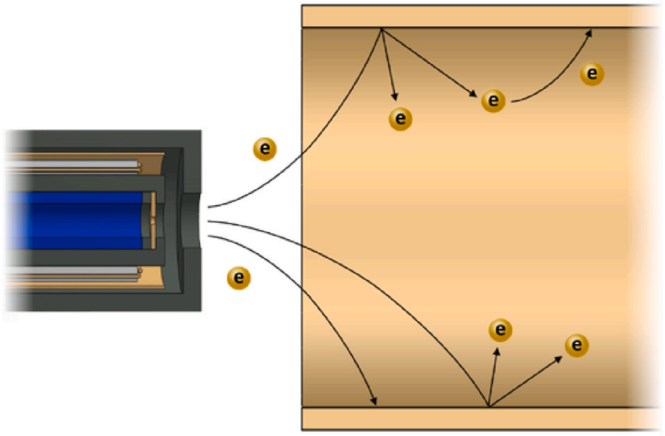

Fig. 15. Accelerated electrons increase the number of secondary electrons at the anode surface.

current regime with the presence of a magnetic field, can be attributed to the deflection of drifting ions in the plume region by the transverse magnetic field, leading to a decreased local ion density and eventually reducing the IAT. Recent developments in the modeling and experimentation of HCs have shown that the emergence of the IAT at higher discharge currents or low mass flow rates can induce coherent ionization-like instabilities, i.e., large-scale oscillations with frequencies below 150 kHz. A clear correlation has been established between the IAT and ionization-like instabilities in cathode plume mode discharge [62–64]. The presence of a magnetic field has been observed to mitigate the IAT in cathode discharges, which can explain a decrease in the PSD of low-frequency ionization-like instabilities below 150 kHz.

4.4. Plots of the discharge voltage versus the argon flow rate

The relationship between the discharge voltage and the argon flow rate in SCCM units is presented in Fig. 17. In the absence of a magnetic field, the discharge voltage of the HC is 29.9 V at 7 SCCM with an 8 A discharge current, while the discharge voltage with a magnetic field at the same operating condition is 31.3 V. The HC with a magnetic field can operate in a self-heating condition at a minimum gas flow rate of 4 SCCM with an 8 A discharge current. On the other hand, the HC without a magnetic field can operate at a discharge current of 2 SCCM under the same conditions.

In the high argon flow rate regime, the discharge voltage tends to decrease regardless of the presence of an octupole magnet, which can be attributed to the increase in emitter temperature during operation [39]. With the increase in propellant flow rate, the plasma drift resistance in the orifice region, specifically the orifice of the molybdenum plate, also increases. The plasma encounters high resistance as it passes through the orifice, leading to increased collisions between charged particles, producing significant resistive heating in the orifice plasma. This ohmic

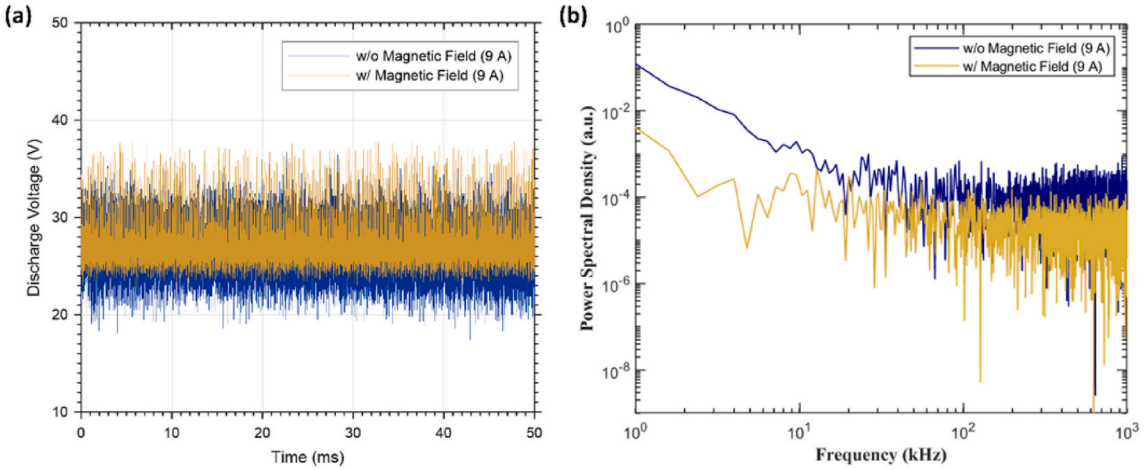

Fig. 16. Plots of (a) time-varying waveforms and (b) power spectral density at the discharge current of 9 A with the gas flow rate of 7 SCCM.

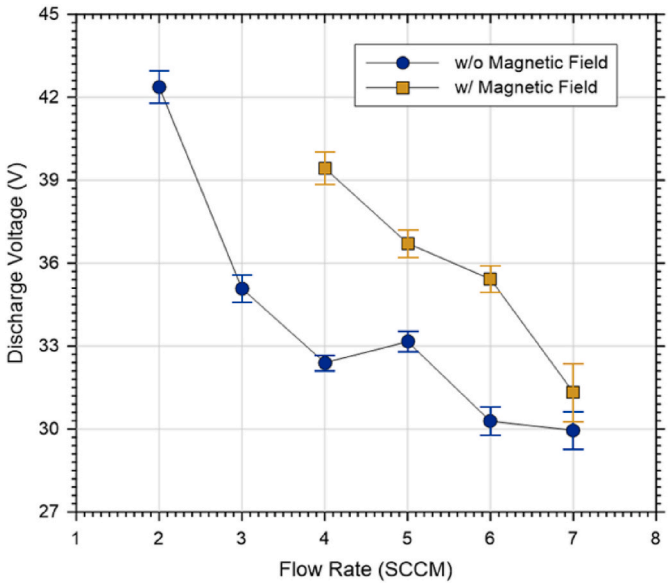

Fig. 17. Plot of the discharge voltage versus the argon flow rate at a nominal discharge current of 8 A.

power is then convectively transferred to the orifice plate through plasma bombardment and eventually heated the insert through conduction and radiation.

As the gas flow rate increases, the pressure within the cathode also increases, causing a shift in the heating mechanism from ion bombardment heating to electron bombardment and orifice heating [38]. Ion bombardment heating occurs when ions in the cathode insert region fall through the sheath potential at the insert surface, leading to surface heating by ion bombardment. On the other hand, electron bombardment heating is enhanced with relatively high internal cathode pressure, which results in decreased electron temperatures and sheath potentials; this allows some energetic electrons to surpass the sheath potential and reach the insert surface, depositing their kinetic energy and keeping it at the thermionic emission temperature. The reduced sheath potentials simultaneously mitigate the ion bombardment heating in the cathode.

The discharge *I–V* curve depicted in Fig. 17 indicates that, over its operating flow rate range, the discharge voltage in the presence of a magnetic field is higher than that in the absence of a magnetic field, ranging from 1.37 to 7.04 V. This can be attributed to the transverse magnetic field in the plume region, as illustrated in Fig. 9, which increases the drift resistance of low-energy electrons and, consequently, raises the discharge voltage to a sufficient level that can attract electrons to sustain the main discharge. Fig. 18(a) and (b) show plots of the peak-to-peak discharge voltage and the amplitude of the discharge voltage oscillation versus the cathode flow rate, respectively.

The substantial voltage fluctuation observed in the low-flow-rate regime has been attributed to the emergence of the IAT [34,60,61]. When the gas flow rate is reduced to 2 SCCM without the presence of a magnetic field, the peak-to-peak discharge voltage is measured at 16.9 V, with an amplitude of the discharge voltage oscillation at 1.15 V. Meanwhile, when the magnetic field is introduced to the HC discharge, and the flow rate is increased to 4 SCCM at a same discharge current, the peak-to-peak discharge voltage is 11.2 V with an amplitude of the discharge voltage oscillation at 1.14 V. Fig. 19 presents the time-varying waveforms and the PSD analysis of the 2 and 4 SCCM discharge.

The time-varying waveforms show that the HC's discharge voltage operating at 2 SCCM is 9.9 V higher than that at 4 SCCM, while the discharge voltage at 4 SCCM with magnetic field coupling is 7.03 V higher than that without. The PSD analysis revealed that the discharge at 2 SCCM had a more energetic spectrum compared to that at 4 SCCM, with the former exhibiting a more energetic high-frequency IAT (more than 200 kHz) and low-frequency plume mode oscillation (below 150 kHz). The discharge with and without magnetic field at 4 SCCM showed similar spectra.

Fig. 18 demonstrates that when the flow rate is set at 7 SCCM, the presence of magnetic field results in a significant increase in both peak-to-peak discharge voltage and amplitude of discharge voltage oscillation. Specifically, these values were found to be 4.6 V and 0.71 V higher, respectively, than those recorded without the magnetic field. Time-varying waveforms and PSD analysis were performed, presented in Fig. 20. The discharge waveform of the HC with the external octuple magnetic field was observed to exhibit a noticeable periodic oscillation with a large amplitude in discharge voltage compared to the waveform of the HC without the magnetic field. Additionally, the PSD analysis of the discharge coupling with the magnetic field at 7 SCCM showed a spike of high energy spectra in the range of 60–110 kHz; this is linked to the increase of the low-frequency ionization-like plume mode oscillation, while the PSD in the high-frequency domain shared a similar spectrum.

The higher discharge oscillation observed in the presence of the octupole magnetic field at high flow rates can be attributed to the accumulation of electrons at the periphery of the keeper, as illustrated in Fig. 21. At higher gas flow rates, the electron energy at the keeper orifice periphery is reduced due to collisions with the higher density of neutral particles. As a result, low-energy electrons are confined by the transverse magnetic field, as shown in Fig. 9, causing an increase in ionization-like instabilities in the plume region, typically observed at

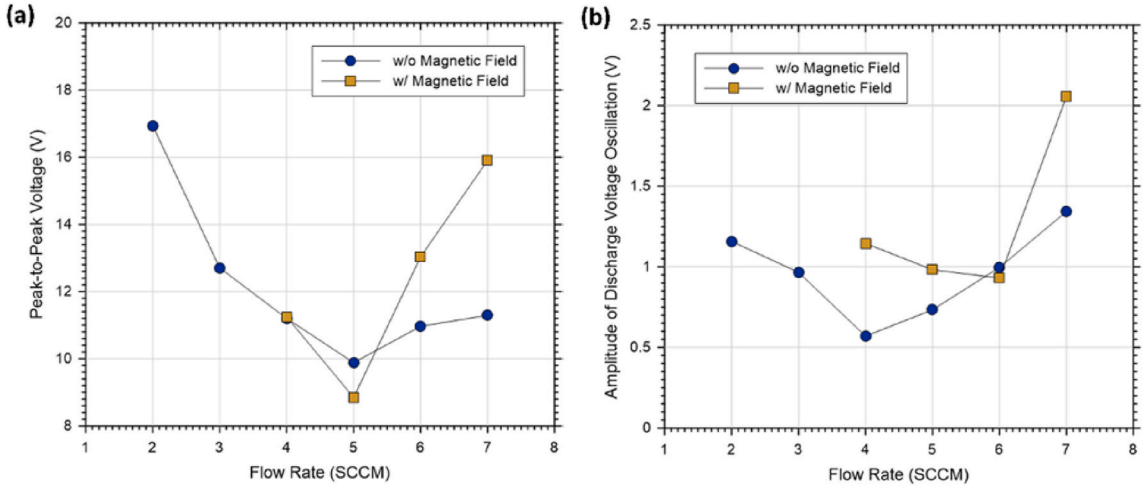

Fig. 18. Plots of the (a) peak-to-peak voltage and (b) amplitude of the discharge voltage oscillation versus the argon flow rate at a nominal discharge current of 8 A.

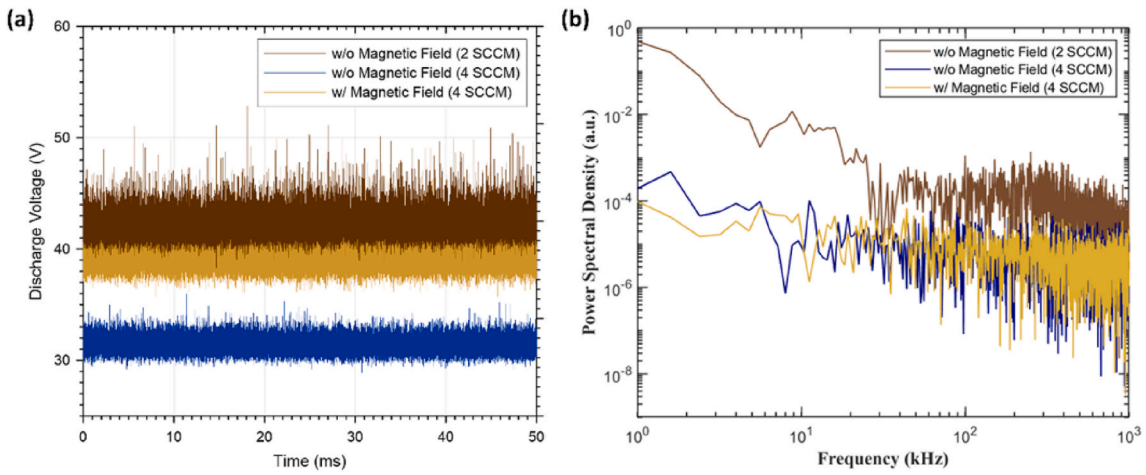

Fig. 19. Plots of (a) time-varying waveforms and (b) power spectral density of the hollow cathode discharge at 2 and 4 SCCM with an 8 A discharge current.

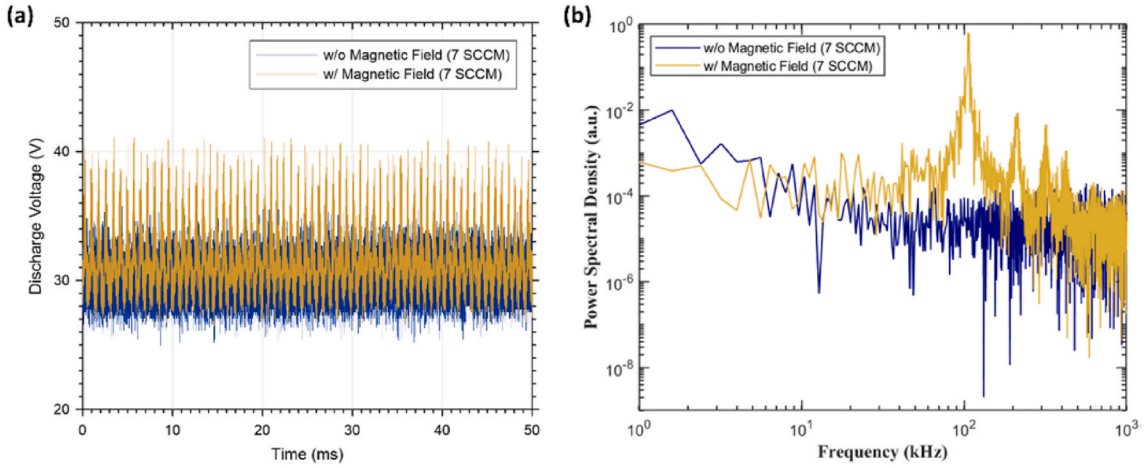

Fig. 20. Plots of (a) time-varying waveforms and (b) power spectral density of the hollow cathode discharge at 7 SCCM with an 8 A discharge current.

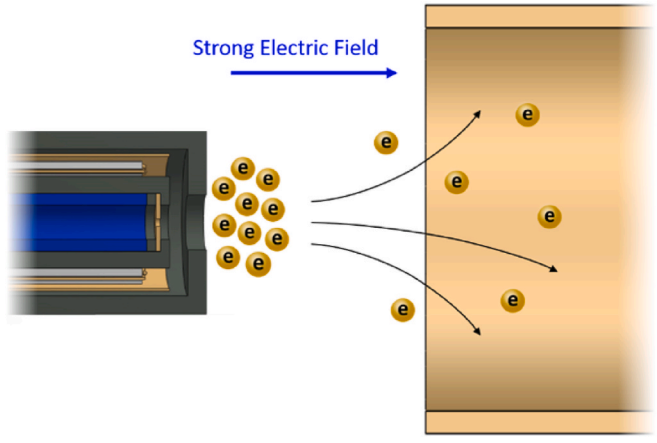

Fig. 21. Acumulated electrons and enhanced electric field between the keeper and the anode.

low flow rates or large discharge currents [54]. Additionally, the accumulated electrons lead to a stronger electric field towards the anode, accelerating the electrons at the middle and downstream ends of the plume region where the neutral density is relatively low and collision rates are reduced. The accelerated electrons at the middle and downstream ends impact the anode surface with higher kinetic energy, thereby increasing the number of secondary electron yields at the anode and increasing the discharge voltage oscillation accordingly.

4.5. *Post-test examination*

After experiments, the cathode was subjected to a post-test to ensure that the LaB6 emitter did not degrade or become contaminated by propellant impurities and refractory metal. The discharge voltage versus discharge current during the post-test was consistent with the result before the experiment. Considering heater failure is one of the most common EP malfunctions in space, the cathode was uninstalled from the vacuum chamber and disassembled after the post-test to evaluate the degradation of the heater. Fig. 22 depicts portions of the alumina insulator tube that melted due to the overheating of the molybdenum wire. Because of the thermal fatigue and delayed shutdown of the heater when the cathode was ignited, this excessive temperature might be relevant to the extremely high temperature of the heater wire. Presumably, a portion of the molybdenum heater wire was exposed through the melting region of the alumina tube, which increased the likelihood of a short circuit with the radiation-shielding molybdenum foil. However, this problem can be resolved by increasing the thickness of the alumina tube, substituting the alumina insulator with a better heat-resistant material (e.g., boron nitride), or implementing a heating process without a heater in the subsequent version of the cathode.

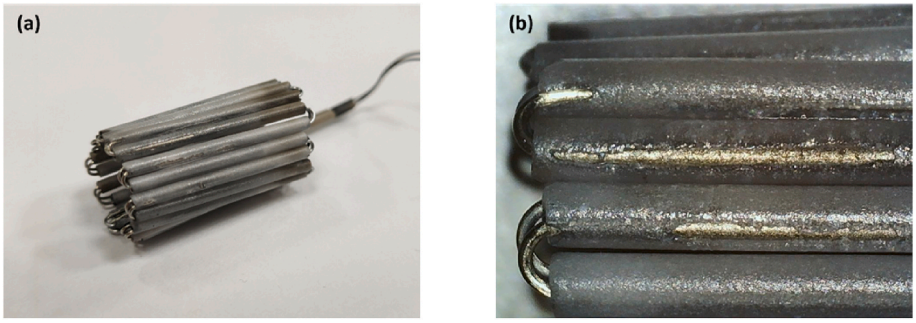

Fig. 22. (a) Heater and (b) melted alumina insulator tube.

5. Conclusion

This paper describes the design and development of a LaB6 HC for the MOPT. It also investigates the discharge characteristics of this cathode, which was designed to be mounted at the center of the thruster in the presence of an octupole magnet.

Throughout the experiments, a negative correlation was observed between the discharge voltage and the cathode current, ascribed to the low sheath potential in the insert region and the high temperature of the emitter. The study found that the presence of the octupole magnetic field slightly increased the discharge voltage in the high-discharge-current regime. This increase was attributed to a portion of low-energy electrons being trapped by the transverse magnetic field in the plume region, which required a higher voltage to sustain the main discharge. In the absence of the octupole magnet, the discharge voltage oscillation of the cathode considerably increased in both the low-discharge-current and high-discharge-current regimes. The PSD analysis revealed that ionization-like instabilities were enhanced in the low discharge current regime, while a more energetic spectrum existed in the high discharge regime, but both were mitigated due to the presence of an external octupole magnetic field.

The results also showed that the discharge voltage was anti-correlated with the argon flow rate, attributed to the increased drift resistance in the orifice region, which increased the emitter temperature during cathode operation. The large plasma instabilities in the low-flow-rate regime were linked to the IAT's emergence, enhancing the ionization-like instabilities in the low-frequency domain. According to the PSD analysis, a spike of an energetic spectrum was observed in the range of 60–110 kHz in the high-flow-rate regime with the presence of the magnetic field, indicating the enhacnement of the ionization-like instabilities. Additionally, the high magnetic-field-induced discharge voltage oscillation observed in the high-flow-rate regime was presumably caused by the accumulation of electrons at the periphery of the keeper, eventually increasing the secondary electron yield at the anode surface.

Afterward, the cathode was uninstalled from the vacuum chamber and disassembled to examine the degradation of each of its components. In general, a melted alumina tube is one of the most obvious types of degradation in heater insulation. In order to increase the lifetime of HCs, a HC without a heater is under consideration in a subsequent project. In conclusion, the present research represents a crucial step in the development of a LaB6 HC for the MOPT for future space applications.

CRediT authorship contribution statement

Jordan H. Hsieh: Writing – original draft, Methodology, Formal analysis, Conceptualization. **Mitchell M. Shen:** Writing – original draft, Validation, Supervision. **Yueh-Heng Li:** Writing – original draft, Supervision, Resources, Project administration, Funding acquisition. **Ping-Han Huang:** Writing – review & editing.

Declaration of competing interest

The authors declare that they have no known competing financial interests or personal relationships that could have appeared to influence the work reported in this paper

Data availability

Data will be made available on request.

Acknowledgement

This work was supported by the Ministry of Science and Technology (Taiwan) [MOST 109-2221-E-006-037-MY3, MOST 110-2622-E-006-029] and National Science and Technology Council (Taiwan) [NSTC 111-2224-E-006-008].

References

[1] D. Rafalskyi, J.M. Martínez, L. Habl, E. Zorzoli Rossi, P. Proynov, A. Boré, T. Baret, A. Poyet, T. Lafleur, S. Dudin, In-orbit demonstration of an iodine electric propulsion system, Nature (2021) 1–5.
[2] H. Watanabe, S. Cho, K. Kubota, Performance and plume characteristics of an 85 W class Hall thruster, Acta Astronaut. 166 (2020) 227–237.
[3] T.-Y. Huang, Y.-H. Li, M.-H. Shen, Y.-C. Chen, Development of a miniature radio-frequency ion engine with inductively coupled plasma (ICP) source for cube satellite propulsion, AIAA Propulsion and Energy 2021 Forum (2021) 3417.
[4] Y.-H. Li, K. Dorn, H.-C. Hsieh, T.-C. Kuo, Y.-C. Hsu, Effect of electrode angle on pulsed plasma thruster performance, Journal of Aeronautics, Astronautics and Aviation 53 (3) (2021) 353–367.
[5] D. Goebel, I. Katz, J. Ziemer, J. Brophy, J. Polk, L. Johnson, A. Sengupta, Electric propulsion research and development at JPL, in: 41st AIAA/ASME/SAE/ASEE Joint Propulsion Conference & Exhibit, 2005, p. 3535.
[6] J. Hsieh, Y. Li, M. Shen, Y.-L. Huang, Cylindrical magnetic quadrupole plasma thruster with a filament emitter hollow cathode, in: 37th International Electric Propulsion Conference, 2022, p. 437.
[7] M. Huang, W.Y.L. Ling, S. Zhang, X. Liu, N. Wang, Spectroscopic plasma plume study of a non-volatile liquid-fed pulsed plasma thruster, Acta Astronaut. 198 (2022) 76–86.
[8] P. Hu, Y. Shen, Z. Yao, W. Mao, Y. Hu, X. Liu, Study of multi-cusped plasma thruster applied to Air-Breathing Electric Propulsion, Vacuum 190 (2021), 110275.
[9] B.-H. Huang, Y.-H. Li, H.-Y. Lee, J.H. Hsieh, Development of a new vacuum arc thruster with multilayer electrodes, AIAA Propulsion and Energy 2021 Forum (2021) 3436.
[10] N. Meckel, R. Cassady, R. Osborne, W. Hoskins, R. Myers, Investigation of pulsed plasma thrusters for spacecraft attitude control, in: Proc. Of 25th International Electric Propulsion Conference, IEPC-97-128, 1997. Cleveland, Ohio.
[11] Y.-H. Li, C. Royer, Effect of voltage on second-stage electrodes of dual-stage solid propellant pulsed plasma thruster, Vacuum 167 (2019) 103–112.
[12] Y.-H. Li, S. Palagiri, P.-Y. Chang, C. Montag, G. Herdrich, Plasma behavior in a solid-fed pulsed plasma thruster, J. Aeronaut. Astronaut. Aviat. 51 (1) (2019) 31–42.
[13] Y.-H. Li, J.-Y. Pan, G. Herdrich, Design and demonstration of micro-scale vacuum cathode arc thruster with inductive energy storage circuit, ACTA Astronaut. 172 (2020) 33–46.
[14] M. Tajmar, A. Genovese, W. Steiger, Indium field emission electric propulsion microthruster experimental characterization, J. Propul. Power 20 (2) (2004) 211–218.
[15] R. Cassady, N. Meckel, W. Hoskins, R. Myers, S. Oleson, M. McGuire, Pulsed Plasma Thruster Systems for Spacecraft Attitude Control, 1996.

[16] Y.-H. Li, Y.C. Chen, S.-W. Liu, A.R. Aslan, Prediction and optimization of thrust performance from plasma diagnostics in the inductively coupled plasma of an RF ion thruster, ACTA Astronaut. 208 (2023) 130–141.
[17] Y.-H. Li, T.-Y. Huang, M.M. Shen, Y.-C. Chen, Development of miniature radio frequency ion thruster with inductively coupled plasma source, J. Aeronaut. Astronaut. Aviat. 55 (1) (2023) 13–28.
[18] D.M. Goebel, J. Crow, A. Forrester, Lanthanum hexaboride hollow cathode for dense plasma production, Rev. Sci. Instrum. 49 (4) (1978) 469–472.
[19] B. Arkhopov, K. Kozubsky, The development of the cathode compensators for stationary plasma thrusters in the USSR, in: 22nd International Electric Propulsion Conference, 1991, pp. 14–17, paper IEPC-91-023, Viareggio, Italy Oct.
[20] D. Goebel, Y. Hirooka, T. Sketchley, Large-area lanthanum hexaboride electron emitter, Rev. Sci. Instrum. 56 (9) (1985) 1717–1722.
[21] R. Albertoni, D. Pedrini, F. Paganucci, M. Andrenucci, Experimental characterization of LaB6 hollow cathode for low-power Hall effect thrusters, Proceedings of the Space Propulsion Conference (SP) (2014) 19–22.
[22] A. Daykin-Iliopoulos, I. Golosnoy, S. Gabriel, Thermal Profile of a Lanthanum Hexaboride Heaterless Hollow Cathode, 2017.
[23] D. Pedrini, R. Albertoni, F. Paganucci, M. Andrenucci, Development of a LaB6 cathode for high-power Hall thrusters, in: 34th International Electric Propulsion Conference, 2015.
[24] D.M. Goebel, R.M. Watkins, Compact lanthanum hexaboride hollow cathode, Rev. Sci. Instrum. 81 (8) (2010), 083504.
[25] R. Joussot, L. Grimaud, S. Mazouffre, Examination of a 5 A-class cathode with a LaB6 flat disk emitter in the 2 A–20 A current range, Vacuum 146 (2017) 52–62.
[26] A. Daykin-Iliopoulos, I.O. Golosnoy, S. Gabriel, Development of a High Current Heaterless Hollow Cathode, 2018.
[27] Z.-X. Ning, H.-G. Zhang, X.-M. Zhu, L. Ouyang, X.-Y. Liu, B.-H. Jiang, D.-R. Yu, 10000-ignition-cycle investigation of a LaB 6 hollow cathode for 3–5-kilowatt Hall thruster, J. Propul. Power 35 (1) (2019) 87–93.
[28] G. Becatti, D.M. Goebel, 500-A LaB6 Hollow cathode for high power electric thrusters, Vacuum 198 (2022), 110895.
[29] A. Daykin-Iliopoulos, I.O. Golosnoy, S. Gabriel, F. Bosi, Characterisation of a 30 A Heaterless Hollow Cathode, 2019.
[30] R.W. Conversano, G. Becatti, D.M. Goebel, V.H. Chaplin, Demonstration of 13,011-h of operation of a proto-flight compact heaterless lanthanum hexaboride hollow cathode, Acta Astronaut. 197 (2022) 53–59.
[31] D.M. Goebel, J.E. Polk, Lanthanum hexaboride hollow cathode for the asteroid redirect robotic mission 12.5 kW Hall thruster, in: Joint 30th ISTS, 34th IEPC and 6th NSAT Conf, 2015. Hyogo-Kobe, Japan, 4–10 July 2015.
[32] D.M. Goebel, R.M. Watkins, K.K. Jameson, LaB6 hollow cathodes for ion and Hall thrusters, J. Propul. Power 23 (3) (2007) 552–558.
[33] D.M. Goebel, G. Becatti, I.G. Mikellides, A. Lopez Ortega, Plasma hollow cathodes, J. Appl. Phys. 130 (5) (2021), 050902.
[34] M. Georgin, Ionization Instability of the Hollow Cathode Plume, 2020.
[35] B.A. Jorns, R.R. Hofer, Plasma oscillations in a 6-kW magnetically shielded Hall thruster, Phys. Plasmas 21 (5) (2014), 053512.
[36] S. Tsikata, K. Hara, S. Mazouffre, Characterization of hollow cathode plasma turbulence using coherent Thomson scattering, J. Appl. Phys. 130 (24) (2021), 243304.
[37] G. Becatti, D.M. Goebel, M. Zuin, Observation of rotating magnetohydrodynamic modes in the plume of a high-current hollow cathode, J. Appl. Phys. 129 (3) (2021), 033304.
[38] D.M. Goebel, I. Katz, Fundamentals of Electric Propulsion: Ion and Hall Thrusters, John Wiley & Sons, 2008.
[39] D.M. Goebel, I. Katz, Fundamentals of Electric Propulsion: Ion and Hall Thrusters, John Wiley & Sons, 2008.
[40] V. Khayms, M. Martinez-Sanchez, Design of a Miniaturized Hall Thruster for Microsatellites, 32nd Joint Propulsion Conference and Exhibit, 1996, p. 3291.
[41] E. Choueiri, Fundamental difference between the two Hall thruster variants, Phys. Plasmas 8 (11) (2001) 5025–5033.
[42] S. Mazouffre, S. Tsikata, J. Vaudolon, Development and experimental characterization of a wall-less Hall thruster, J. Appl. Phys. 116 (24) (2014), 243302.
[43] Y. Ding, H. Li, H. Sun, L. Wei, B. Jia, H. Su, W. Peng, P. Li, D. Yu, A 200-W permanent magnet Hall thruster discharge with graphite channel wall, Phys. Lett. 382 (42–43) (2018) 3079–3082.
[44] M. Ding, H. Li, Y. Ding, L. Wei, W. Mao, D. Yu, Y. Cao, Performance and plume characteristics of a Hall-effect thruster with asymmetrical gas supply, Vacuum 190 (2021), 110285.
[45] J.H. Hsieh, Y.-H. Li, M. Shen, W.-C. Lien, P.-H. Lin, Hectowatt-Class Double-Peaked Hall Thruster for Future Space Missions, in: 37th International Electric Propulsion Conference, IEPC-2022-394, 2022.
[46] J. Boldeman, D. Einfeld, The physics design of the Australian synchrotron storage ring, Nucl. Instrum. Methods Phys. Res. Sect. A Accel. Spectrom. Detect. Assoc. Equip. 521 (2–3) (2004) 306–317.
[47] D.J. Warner, Advanced Cathodes for Next Generation Electric Propulsion Technology, AIR FORCE INST OF TECH WRIGHT-PATTERSON AFB OH SCHOOL OF ENGINEERING AND, 2008.
[48] G.A. Csiky, Measurements of Some Properties of a Discharge from a Hollow Cathode, National Aeronautics and Space Administration, 1969.
[49] G.-C. Potrivitu, S. Mazouffre, L. Grimaud, R. Joussot, Anode geometry influence on LaB6 cathode discharge characteristics, Phys. Plasmas 26 (11) (2019), 113506.
[50] T. Jack, S. Patterson, D. Fearn, The effect of the keeper electrode on hollow cathode discharge characteristics, in: 36th AIAA/ASME/SAE/ASEE Joint Propulsion Conference and Exhibit, 2000, p. 3533.
[51] G. Becatti, R.W. Conversano, D.M. Goebel, Demonstration of 25,000 ignitions on a proto-flight compact heaterless lanthanum hexaboride hollow cathode, Acta Astronaut. 178 (2021) 181–191.
[52] A. Riccardo, A. Mariano, D. Pedrini, F. Paganucci, Preliminary characterization of a LaB6 hollow cathode for low-power Hall effect thrusters, in: 33rd International Electric Propulsion Conference, 2013.
[53] N. Yamamoto, K. Komurasaki, Y. Arakawa, Discharge current oscillation in Hall thrusters, J. Propul. Power 21 (5) (2005) 870–876.
[54] D.R. Lev, I.G. Mikellides, D. Pedrini, D.M. Goebel, B.A. Jorns, M.S. McDonald, Recent progress in research and development of hollow cathodes for electric propulsion, Reviews of Modern Plasma Physics 3 (2019) 1–89.
[55] G.-C. Potrivitu, L. Xu, S. Huang, M. Rohaizat, S. Xu, Discharge mode transition in a Krypton-fed 1 A-class LaB6 cathode for low-power Hall thrusters for small satellites, J. Appl. Phys. 127 (6) (2020), 064501.
[56] M. Mandell, I. Katz, Theory of Hollow Operation in Spot and Plume Modes, 30th Joint Propulsion Conference and Exhibit, 1994, p. 3134.
[57] L. Cassady, E. Choueiri, Lithium-fed Hollow Cathode Theory, 40th AIAA/ASME/SAE/ASEE Joint Propulsion Conference and Exhibit, 2004, p. 3431.
[58] F.F. Chen, Introduction to Plasma Physics and Controlled Fusion, Springer, 1984.
[59] G.-C. Potrivitu, S. Xu, Evidence of the ionization instability and ion acoustic turbulence correlation in sub-ampere hollow cathodes, Journal of Electric Propulsion 1 (1) (2022) 1–22.
[60] B.A. Jorns, I.G. Mikellides, D.M. Goebel, Ion acoustic turbulence in a 100-A LaB 6 hollow cathode, Phys. Rev. 90 (6) (2014), 063106.
[61] M.P. Georgin, B.A. Jorns, A.D. Gallimore, An experimental and theoretical study of hollow cathode plume mode oscillations, in: 35th International Electric Propulsion Conference, IEPC-2017, 2017.
[62] G. Sary, L. Garrigues, J.-P. Boeuf, Hollow cathode modeling: II. Physical analysis and parametric study, Plasma Sources Sci. Technol. 26 (5) (2017), 055008.
[63] G. Sary, L. Garrigues, J.-P. Boeuf, Hollow cathode modeling: I. A coupled plasma thermal two-dimensional model, Plasma Sources Sci. Technol. 26 (5) (2017), 055007.
[64] B.A.J.M.P. Georgin, A.D. Gallimore, Onset Criterion for a Turbulence-Driven Ionization Instability in Hollow Cathodes, IEPC Paper IEPC-2019-155, 2019.